

Spectroscopy of photoionization from the 1E singlet state in nitrogen–vacancy centers in diamond

Sean M. Blakley,* Thuc T. Mai, Stephen J. Moxim, Jason T. Ryan,
 Adam J. Biacchi, Angela R. Hight Walker, and Robert D. McMichael†
National Institute of Standards and Technology, Gaithersburg, MD 20899 USA

(Dated: January 26, 2023)

The 1E – 1A_1 singlet manifold of the negatively charged nitrogen vacancy (NV^-) center in diamond plays a central role in the quantum information and quantum sensing applications of the NV^- center. However, the energy of this manifold within the diamond bandgap and with respect to the 3A_2 – 3E triplet manifold has not been measured directly. Using field-quenching effects on photoluminescence (PL) spectra, we report on the energy gap between the 1E – 1A_1 singlet manifold and the 3A_2 and 3E ground and excited triplet states of the NV^- as a function of excitation wavelength and power, temperature, and applied magnetic field in a heavily nitrogen-doped sample. Increased PL and decreased zero-phonon line width from the NV^0 were observed in the presence of an applied magnetic field, indicating ionization from the long-lived 1E singlet state. A temperature-dependent ionization threshold between 532 nm and 550 nm was found, locating the singlet states within the diamond band gap.

I. INTRODUCTION

The nitrogen vacancy (NV) center in diamond has emerged as important platform for quantum technology.[1–11] The negative charged state (NV^-) garners the most interest due to its $S = 1$ triplet ground state. These ground state sublevels have long coherence times and can be polarized and read out optically at room temperature.[12, 13].

Initiation and readout of the NV^- spin state involves transitions between four electronic states within the diamond band gap: the ground (3A_2) and excited (3E) electronic states, both $S = 1$ spin triplets, and the metastable (1E) and excited (1A_1) electronic states, both $S = 0$ spin singlets. See Fig. 1(a). For illumination wavelengths between 470 nm and 637 nm, NV^- centers will absorb photons and transition from ground to the excited 3E states and either relax back to the ground state by emitting a photon, or relax via the inter-system crossings (ISCs) and the singlet states. The spin-dependence of the upper ISC makes it possible to prepare the $m_z = 0$ spin state with good fidelity and to read it out via photoluminescence (PL). The lower ISC is a slow process that gives the metastable 1E state a lifetime that is an order of magnitude longer than any other excited state.[6]

The 3A_2 – 3E and 1E – 1A_1 transition energies in the NV^- are determined by the photon energies of the zero phonon lines (ZPL) present in the photoluminescence excitation and PL spectra near 1.95 eV and 1.190 eV respectively.[6, 14–17] The single-photon ionization and recombination thresholds place the NV^- ground state 2.60 eV below the conduction band and 2.94 eV above the valence band.[18]

The 1A_1 – 3E and 3A_2 – 1E energy gaps, labeled Δ

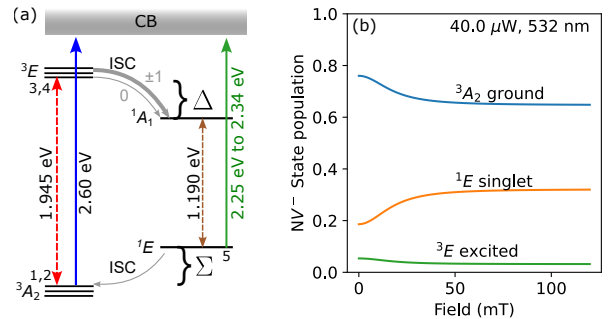


FIG. 1. (a) Diagram of energy levels and transitions in the NV^- center. Energy differences between the 3A_2 ground state and 3E excited states and between the 1E and 1A_1 singlet states are indicated by dashed arrows. Ionization transitions are shown with solid arrows. The ISC across the 3E – 1A_1 energy gap Δ is spin dependent and is primarily responsible for the optically detected magnetic resonance (ODMR) properties of the NV^- centers. The bounds placed on the ionization threshold of the singlet state are a main result of this work. (b) Modeled state populations under constant illumination as a function of field applied along the diamond [001] axis. Ionization from the singlet state is identified by increasing effect with applied field, consistent with increased singlet population.

and Σ respectively in Fig. 1 (a), have proven to be more difficult to measure. Indirect estimates of Δ and Σ at cryogenic temperatures have been provided by calculations relating ISC rates to the Δ and Σ energy differences. Using measured ISC rates, Σ is estimated to be 0.4 eV,[15] and Δ is estimated to lie between 0.321 eV and 0.414 eV.[19–21] Earlier work done at high temperature is at variance with these results, yielding an estimate of $\Delta \approx 0.8$ eV, which implies that $\Sigma \approx 0$ eV[22]. This discrepancy suggests a possible temperature dependence of Δ and Σ .

Determining the photon energy threshold for ionization of the 1E is a more direct method to estimate Δ

* smb784@umd.edu

† robert.mcmichael@nist.gov

and Σ . Ionization of NV^- results in an increase of NV^0 concentration and an increase in NV^0 PL, but it is necessary to isolate ionization from 1E from other pathways. For this purpose, the 1E population has been modulated previously using continuous magnetic resonance[23] and microwave pulses [24–26] Using microwave pulse modulation, Wolf et al. bracket the 1E ionization threshold between 1.91 eV and 2.25 ev, corresponding to 0.35 eV $< \Delta < 0.69$ eV.

Here, we use a steady, off-axis, magnetic field to modulate the 1E population. The off-axis applied field mixes the spin states within the 3A_2 triplet and some population of the 3A_2 is transferred to the 1E singlet (Fig. 1 (b)). The ionization threshold of the 1E is then determined by tuning the wavelength of the excitation laser and recording the change in the NV^0 PL when the magnetic field is turned off.

In the present work, we use field modulation to investigate ionization threshold of the 1E as a function of temperature in a diamond sample with high NV concentration. Samples of this type are suitable for NV ensemble measurements, particularly magnetometry. For photon energies less than the threshold for direct ionization of the 3A_2 , we find that the fraction of NV centers in the NV^- state is approximately constant across the excitation wavelength range, but that the concentration of NV^0 increases by a few percent when a spin-mixing magnetic field is applied, presumably due to increased ionization from the NV^- singlet state. A temperature dependent threshold for the NV^0 contrast between 532 nm and 550 nm places the singlet state 2.25 eV to 3.34 eV below the conduction band.

Section II describes the sample and experimental methods, and outlines the Bayesian analysis we devised for separating NV^0 and NV^- PL spectra from a high NV concentration sample. Section III discusses the measurement results and their interpretation. Finally, Appendix A presents details of the data analysis.

II. METHODS

A. Experimental

The sample is a commercial CVD-grown diamond (3 mm \times 3 mm \times 0.5 mm) with a typical substitutional nitrogen (N_s) fraction $\approx 13 \times 10^{-6}$ (13 ppm) and NV fraction $\approx 4.5 \times 10^{-6}$ (4.5 ppm). Our quantitative electron spin resonance (ESR) measurements[27] determined the ratio of ESR—active $N_s^0:NV^-$ centers was 3.1 to 1.0. ESR results also revealed the presence of NVH^- centers in concentrations similar to NV ($NV^-:NVH^- = 1.1:1.0$), in agreement with extensive characterization of a similar sample.[28] Relatively small responses from additional defect centers were too heavily obscured by the central N_s^0 and NVH^- resonances for a complete analysis. Absence of NV^0 responses agrees with previous measurements[29] and may be explained by strain broadening.[30] Fitting to

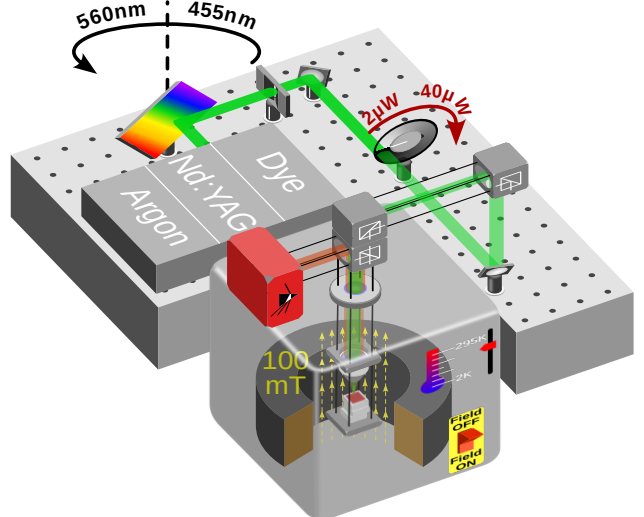


FIG. 2. Diagram of the experimental setup.

ESR simulations of the defects, when necessary, was done with EasySpin software[31] using spin-system parameters taken from several sources.[32–34] The quantitative ESR measurements contain at most 15 % error.

The apparatus for photoluminescence measurement is illustrated in (Fig. 2). The sample is mounted inside a closed-loop, cryogen-free cryostat with an optical window and superconducting magnet. The cryostat is capable of temperatures down to 1.6 K and applied magnetic field up to 9 T. The sample is oriented with the applied field parallel to the [100] crystal axis of the diamond, $\approx 55^\circ$ away from the N-V axes along the [111] direction. Three different continuous wave (CW) lasers are used as a source of excitation for the PL: an argon ion laser generates wavelengths at 458 nm, 476 nm, 488 nm, 497 nm, 502 nm, and 515 nm; a solid state Nd:YAG laser at 532 nm; and a dye laser at 550 nm and 560 nm. Each laser is directed into the cryostat using free space optics. The beam is at normal incidence to the [100] sample surface through a $50\times$ cryogenic objective. The emitted light is collected and sent to two single grating spectrometers, one with a large bandwidth and one with a finer resolution. The laser spot size on the sample is approximately 1 μ m. A continuous variable neutral density filter was used to adjust the power entering the optical window of the cryostat. The optical power was measured by a power meter after the neutral density filter but prior to insertion into the cryostat chamber.

Photoluminescence spectra were collected under CW illumination with ($I_B(\lambda)$) and without ($I_0(\lambda)$) a 100 mT magnetic field. These spectrum pairs were collected for all combinations of nine temperatures from 1.6 K to 295 K, nine laser wavelengths from 458 nm to 560 nm, and five optical powers at 2.5 μ W, 5 μ W, 10 μ W, 20 μ W, and 40 μ W for a total of 405 spectrum pairs.

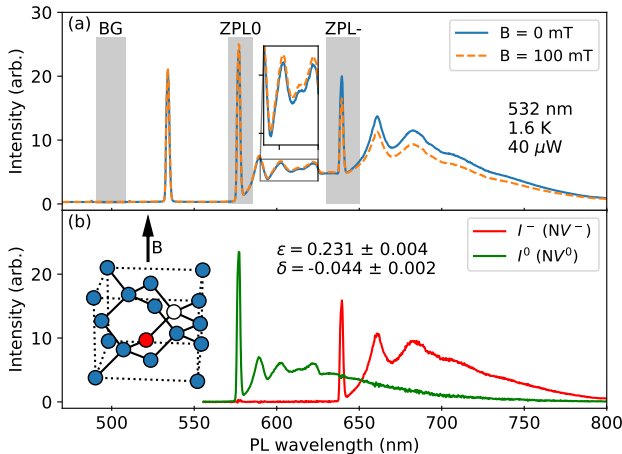


FIG. 3. (a) Example spectra showing the combined photoluminescence of NV^0 and NV^- with applied fields of 0 mT and 100 mT. The peak at ≈ 532 nm is the excitation laser. The inset magnifies the boxed data, showing that the NV^0 PL increases with applied field. (b) Example results of Bayesian inference showing the separated spectra of NV^0 and NV^- labeled I^0 and I^- respectively. Inset: The magnetic field is along the 001 direction, at an angle of $\approx 55^\circ$ from all NV axes, which are along [111] directions.

B. Data Analysis

For samples with large numbers of NV centers, a PL spectrum collected in the presence of either resonant microwave or magnetic field stimulus is subtracted from a subsequent spectrum collected in the absence of this stimulus. This difference spectrum is then used to separate the contribution of the NV^0 , whose PL is largely unaffected by the stimulus, from the NV^- , which is more significantly affected by the stimulus.

To tackle the analysis of our spectrum pairs, we required a reliable technique that can be automated with a minimum of human intervention. We addressed this requirement by developing a Bayesian analysis that separates the contributions of the NV^0 and NV^- through their differing responses to changes in the spin state.[23, 35] The spectra are modeled with zero-field photoluminescence intensity contributions $I^-(\lambda)$ and $I^0(\lambda)$ from NV^- and NV^0 respectively.

$$I_0(\lambda) = I^-(\lambda) + I^0(\lambda) + C + \eta_0, \quad (1)$$

where we have added a constant background C and a measurement noise η_0 . We use quenching parameters ϵ and δ to describe the fractional decrease in PL intensity from the NV^- and NV^0 respectively due to the spin-mixing effects of the applied field.

$$I_B(\lambda) = (1 - \epsilon)I^-(\lambda) + (1 - \delta)I^0(\lambda) + C + \eta_B, \quad (2)$$

including background C and an uncorrelated noise η_B . Negative values of ϵ or δ indicate intensity that increases with applied field.

Figure 3(a) shows PL spectra from an ensemble of NV centers with the separated contributions of NV^0 and NV^- in panel (b). Each spectrum consists of a narrow, zero-phonon line (ZPL) and several broad features in a phonon band. The analysis determines probability distributions for ϵ , δ and separates the PL intensities $I^-(\lambda)$ and $I^0(\lambda)$. The shaded rectangles in figure 3(a) highlight the regions of the spectra where additional assumptions can be incorporated in the Bayesian analysis. We assume that region BG contains background C only, that region ZPL0 contains only $I^0(\lambda)$, with $I^-(\lambda) = 0$. In region ZPL-, we assume that $I^0(\lambda)$ is a linear function to distinguish it from the sharply peaked structure of $I^-(\lambda)$. Figure 3(b) shows the separated example spectra. The procedure was repeated for 405 field on/off pairs of PL spectra, each yielding values of ϵ , δ and integrate intensities of NV^0 and NV^- PL spectra. Details of the procedure are provided in Appendix A.

We also looked for changes in the width of the NV^- zero phonon line using our high-resolution spectrometer, but we were limited to excitation wavelengths 515 nm and lower by scattered laser light. In a first pass, least-square fits of the NV^0 ZPL to Lorentzian line shapes yielded line widths approximately 0.25 nm up to 100 K, then increasing to 1.5 nm at 300 K. Systematic misfit between the Lorentzian model and the peak data led to inflated uncertainty estimates. To avoid this problem, the field-induced line width contrast was estimated using a model-free approach that amounts to finding the transformation that best mapped the $B = 0$ mT data onto a cubic spline interpolation of the $B = 100$ mT data. The transformation included "horizontal" expansion of the λ axis around the approximate peak center by a factor of $(1 + \alpha)$, translation of the λ axis to correct the center value, and "vertical" scaling of the $I_0(\lambda)$ axis. For each data point, the difference between the scaled $B = 0$ mT data and the interpolation of the $B = 100$ mT data is essentially an error that determines the likelihood of the scaling parameters given the data values.

C. Modeling

The populations of the NV states are calculated using a five-state model for NV^- and a two-state model for NV^0 .[14, 25, 36–38] The five-state model of NV^- includes transitions between the $m_z = 0$ and combined $m_z = \pm 1$ spin states of 3A_2 electronic state, the the $m_z = 0$ and combined $m_z = \pm 1$ spin states of the 3E level and the long lived 1E singlet state. The 1A_1 state is ignored because of its very short lifetime. The NV^0 is modeled using its ground and excited states. We assume that ionization and recombination rates are slow compared to the internal dynamics of each center, so that the steady state populations of the centers' states are independent of the centers' concentrations. See Appendix B for details.

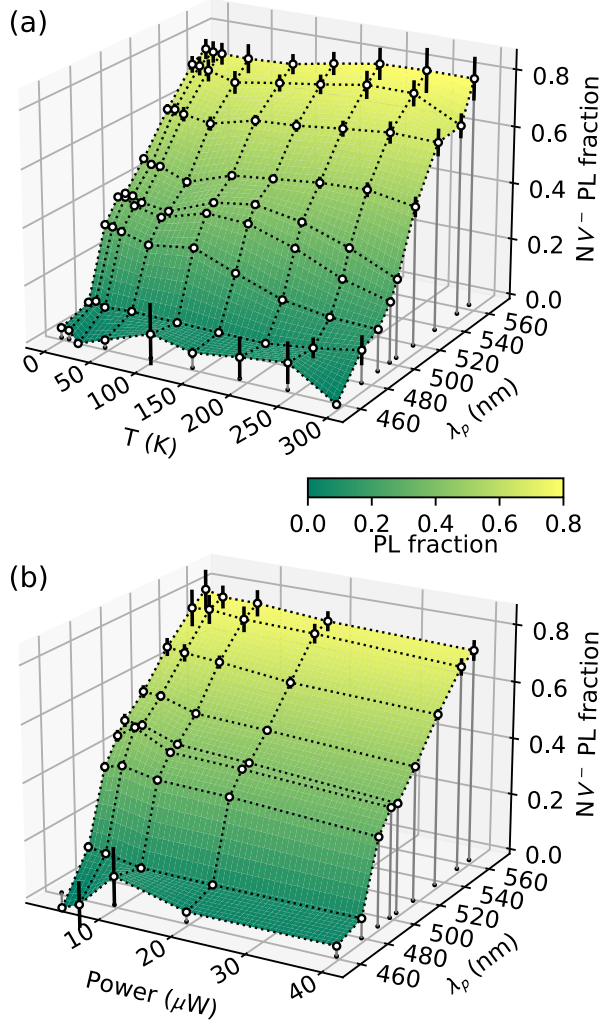


FIG. 4. Fraction of photoluminescence due to NV⁻. (a) PL fraction vs. temperature and wavelength at 40 μW laser power and (b) PL fraction as a function power and wavelength at 1.6 K. In both panels the red line is a model result assuming fixed NV⁻ population fraction $[\text{NV}^-]/[\text{NV}] = 0.67$ and wavelength dependent excitation cross sections.

III. RESULTS AND DISCUSSION

The relative intensity of NV⁻ and NV⁰ photoluminescence yields information about the charge state of NV centers. The fraction of the integrated PL intensity contributed by NV⁻ in zero applied field is plotted in fig 4. Figs. 4 (a) and (b) both show a dropoff in NV⁻ PL intensity between 476 nm and 488 nm (2.605 eV and 2.55 eV resp.). This threshold is consistent with ionization of NV⁻ from its ground state to NV⁰ with a threshold near 2.6 eV (477 nm) at room temperature.[18] Other estimates of the ionization threshold include ab initio calculations of 2.67 eV,[39] and 2.7 eV.[40] The threshold for ionization appears to shift to lower energies and/or broaden at the higher temperatures. A slight decreasing trend with power at all excitation wavelengths in panel

(b) shows that the NV⁻ PL fraction is only weakly power dependent. We next compare the measured PL fraction with several models of charge dynamics all of which assume that the integrated PL intensity for NV⁰ and NV⁻ are proportional to the species concentration and the excited state populations

$$\int I^-(\lambda) d\lambda \propto c_{\text{NV}^-} n_{\text{ex}}^-(\lambda_p) \quad (3)$$

$$\int I^0(\lambda) d\lambda \propto c_{\text{NV}^0} n_{\text{ex}}^0(\lambda_p) \quad (4)$$

where respectively c_{NV^-} , c_{NV^0} , and $n_{\text{ex}}^-(\lambda_p)$, $n_{\text{ex}}^0(\lambda_p)$ are the concentrations and excited state populations of NV⁻ and NV⁰ centers as a function of pumping wavelength λ_p .

A simple “balanced rate” photodynamic model assumes that the rates of ionization and recombination must be equal in the steady state,

$$c_{\text{NV}^-} \Gamma_{\text{NV}^-} = c_{\text{NV}^0} \Gamma_{\text{NV}^0} \quad (5)$$

where Γ_{NV^-} and Γ_{NV^0} are the ionization rate of NV⁻ and recombination rate of NV⁰, respectively. For excitation wavelengths greater than 490 nm and powers on the order of 10 μW , the transition rates are quadratic in laser power and on the order of 10^3 s^{-1} .[18]. The transition rates are modeled as

$$\Gamma_{\text{NV}^-} = J(n_{\text{ex}}^- \sigma_{\text{ex}}^- + n_s^- \sigma_s^- + n_g^- \sigma_g^-) \quad (6)$$

$$\Gamma_{\text{NV}^0} = J(n_{\text{ex}}^0 \sigma_{\text{ex}}^0). \quad (7)$$

for photon flux J and cross sections, σ . Superscripts indicate the charge state of the NV center and subscripts ex , s and g refer to excited, singlet and ground states. Because the populations (other than the ground state) are linear in power, the net ionization and recombination rates are quadratic. Ionization from the ground state is linear in power for excitation below a 485 nm threshold.

We also consider a fixed-concentration model, where the concentrations are only slightly perturbed by quadratic ionization and recombination processes. This model is not physically motivated, but we show in the following that it agrees empirically with our observations.

Figure 5 shows the behavior of rate-balance and fixed-concentration models of as a function of excitation wavelength compared to 1.6 K and 295 K data.

The blue dashed line in fig. 5 is the balanced rate model with ionization allowed only from the excited state. Under this assumption the NV⁻ PL fraction is nearly constant. The green dot-dash curve also includes ionization from the singlet state for wavelengths below 550 nm, and from the ground state below 485 nm. The solid red curve is the fixed-concentration model with $c_{\text{NV}^-} = 0.66$ and $c_{\text{NV}^0} = 0.34$, and the resulting NV⁻ PL fraction increases smoothly across the pump wavelength range.

Qualitative agreement between the fixed-concentration model results and measurement data suggests the NV⁻ and NV⁰ concentrations are approximately unchanged

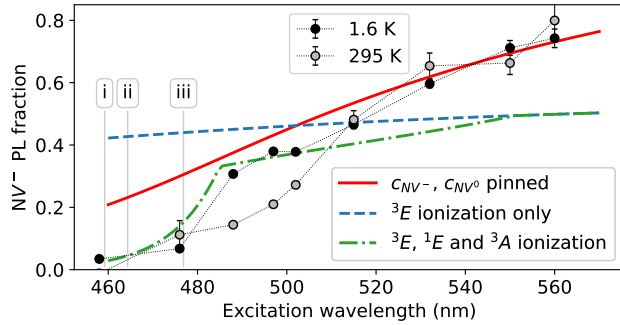


FIG. 5. Fraction of integrated photoluminescence intensity that is due to NV^- as a function of excitation wavelength. Measured data is from 1.6 K (black dots), 295 K (grey dots) and 40 μW excitation power. Error bars indicate one standard deviation. The curves are model results calculated for pinned charge concentrations (solid red line) and for concentrations inversely proportional to ionization rate: using only ionization from the 3E excited state (dashed blue line) and using additional ionization from the 1E singlet and the 3A ground states (dot-dash green line). Ionization thresholds are 551 nm (2.25 eV) from the singlet state and 485 nm for ionization from the ground state. Marked wavelengths are prior estimates of the NV^- ground state ionization threshold. (i) 2.7 eV, calculation, Bouregois et al.,[40] (ii) 2.67 eV, calculation, Razinkovas et al.[39], and (iii) 2.6 eV, ionization rate measurement, Aslam et al.[18]

for excitation wavelengths longer than 490 nm. Below 490 nm, qualitative agreement with the balanced rate model results suggests that ground-state ionization plays an important role. While firm conclusions should not be drawn from these somewhat ad-hoc models, the results are in good agreement with previous measurements of two-step ionization/recombination rates on individual centers.[18] The effects of applied field provide additional information about changes in charge state. The off axis field is known to decrease the population of the 3E excited states and to increase the population of the long-lived singlet state.[6, 35, 37] This shift decreases the PL of NV^- and changes the combined rates of NV^- ionization from the excited and singlet states. In principle the ionization rate could increase or decrease, depending on the corresponding cross sections.

Figure 6(a) shows the contrast parameter ϵ describing a fractional reduction in NV^- PL with applied field as defined in eqns. (1) and (2). The data shows a broad plateau bounded by the ground state ionization threshold near 480 nm, and by a valley of suppressed contrast between 100 K and 1.6 K. Focusing first on the plateau, ϵ is expected to be independent of excitation wavelength in the low-power, linear-response regime as long as concentrations are not wavelength-dependent. The ϵ plot also features a decrease for wavelengths shorter than 490 nm and a prominent valley across all wavelengths between 1.6 K and 100 K. The decrease coincides with depressed NV^- PL shown in fig. 6, and the valley will be discussed

later.

The NV^0 has no known spin-dependent relaxation mechanisms, so its optical properties are considered immune to modest magnetic field. The contrast parameter δ is therefore an indicator of changes in NV^0 concentration. The field-immunity of NV^0 also implies field-independent recombination mechanisms, so we attribute δ to changes in NV^0 concentration due to changes in the NV^- ionization rate. The plot of δ in Fig. 6 (b) shows a region of negative contrast between approximately 500 nm and 560 nm, strongest below 100 K. Negative contrast here corresponds to a field-induced increase in NV^0 PL, implying increased ionization from the 1E singlet state of the NV^- .

As stated above, the population of the excited state decreases with applied field and the population of the singlet state increases, strongly implying that the negative values of δ are due to ionization from the singlet state. This result adds to a growing body of experimental evidence [23–25] that indicates an increase in NV^0 population accompanying an increase in $|\pm 1\rangle$ spin states through steady-state resonance,[23] microwave π pulses,[24, 25] and through DC field quenching (this work).

We do not attempt an explanation for anomalous behavior at 100 K in Fig. 6 (b), which includes the sharp peak at 488 nm and adjacent pit at 497 nm and 502 nm. These anomalies appear consistently over different laser powers and the different wavelengths were measured on different days.

The increase in NV^0 concentration indicated by negative values of δ suggests reactions that reduce the number of charged centers in the diamond. Ionization, $\text{NV}^- \rightarrow \text{NV}^0 + e^-$, neutralizes an NV center, and if the freed electron then goes on to neutralize a N_s^+ ion, the total number of charged centers in the sample is reduced by 2. The accompanying reduction in random electric fields would be observable as a narrowing of ZPL peaks as Stark shift broadening is reduced.

Figure 6(c) shows the fractional change in the width of the NV^0 zero-phonon line with applied field; negative values correspond to narrowing. The results shown fig. 6(c) include a region 488 nm and above and below 150 K where the width of the NV^0 ZPL line decreases by $\approx 2\%$ with applied field, in agreement with the δ contrast for that region. This line width change and the δ contrast both point to significant ionization from the singlet state.

Last, we return to the valley of suppressed ϵ contrast appearing in fig. 6(a) around 50 K and across all wavelengths. A similar valley also appears in results by Rogers et al.[41] We propose an explanation for this effect related to thermal averaging of the excited state orbitals. At room temperature, the excited state behaves like a single spin triplet, but at low temperature the 3E excited state of NV^- is an orbital doublet which is split by transverse strain into 3E_x and 3E_y electronic states separated by tens of GHz.[42, 43] At temperatures above 100 K, these spin triplets are thermally averaged, and the excited state

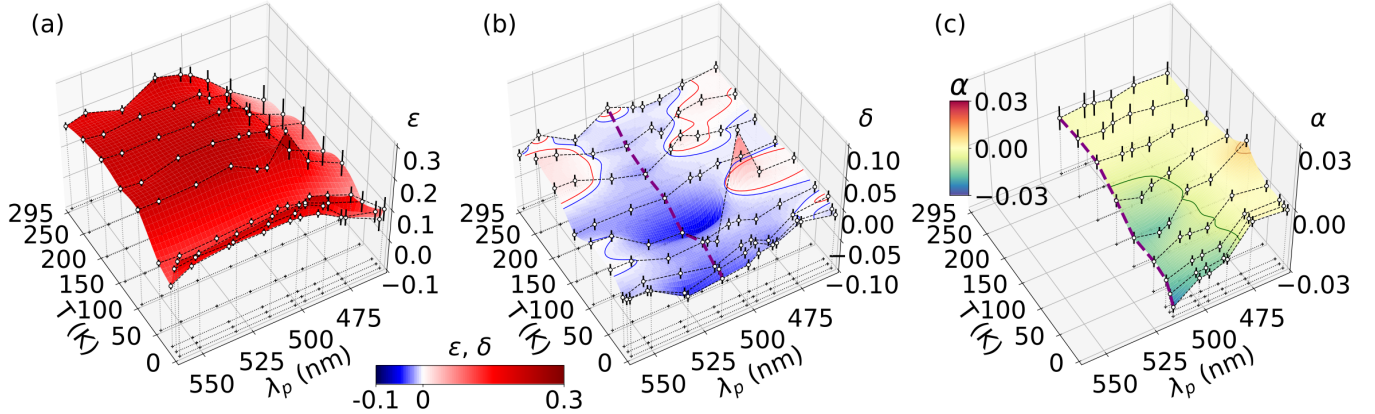


FIG. 6. Field-induced contrast for photoluminescence parameters (a) NV^- intensity ϵ , (b) NV^0 intensity δ , and (c) linewidth α of NV^0 ZPL. Positive (negative) ϵ , δ , and α correspond to decreasing (increasing) (a), (b) PL intensity, and (c) line width respectively under applied field. Solid red, blue curves in (a), (b) and orange, green level curves in (c) represent level curves at two standard deviations above and below zero respectively. Purple dashed line in (b) indicates long wavelength cut-off of the high-resolution spectrometer used to measure linewidths in (c). Color surfaces represent linearly interpolated values between measured data points (white circles with error bars). Black dashed lines connecting data points serve to aid the eye.

appears as one triplet state.[41, 44, 45]. To explain the suppressed contrast, we propose that the thermal averaging process produces an effective field noise that causes fast relaxation of the spin states at intermediate temperatures. The spin relaxation rate will have a maximum when the characteristic switching time is at the GHz frequencies corresponding to transitions between the spin triplet sublevels. This spin-disordering mechanism will oppose pumping into the $m_z = 0$ state. Further mixing and PL quenching due to applied field will have a suppressed effect. In support of this mechanism, we note that shallow minima in the zero-field NV^- PL fraction are visible in the same 50 K neighborhood as the suppressed ϵ contrast. See fig. 4(a). A thorough study of the contrast temperature dependence has recently been made public.[46].

IV. CONCLUSION

The energy gaps Δ and Σ between the $^1E - ^1A_1$ singlet state and the $^3A_2 - ^3E$ triplet state manifolds have been explored as a function of temperature by measuring the photoionization threshold of the 1E state.

For temperatures near 2 K, the ionization threshold was found to be above 560 nm, corresponding to Δ and Σ of 0.36 eV and 0.40 eV respectively, which is in agreement with previous results found in the literature [15, 19–21]. However, these values have not been measured for temperatures between 2 K and 295 K until this work.

For temperatures between 2 K and 200 K, Δ and Σ were found to be similar to the region below 2 K. For temperatures between 200 K and 295 K the 1E ionization threshold was found to be near 532 nm, corresponding to Δ and Σ of 0.48 eV and 0.28 eV respectively, which is more in line with values found in the literature for higher

temperature settings [22, 23]. The results in the 200 K to 295 K region indicate a 0.12 eV shift in energy of the $^1E - ^1A_1$ singlet manifold away from the conduction band, which has not been observed previously.

These results help to resolve inconsistencies in the literature, and will serve as a foundation to develop more effective spin-to-charge conversion techniques going forward.

ACKNOWLEDGMENTS

We wish to acknowledge Ilya Fedotov and Masfer Alkahtani for many helpful discussions and invaluable advice, and Veronika Szalai for initial EPR measurements.

Appendix A: BAYESIAN ANALYSIS

The photoluminescence (PL) spectra are analyzed using Bayesian inference with a the goal of estimating parameters ϵ and δ from arrays of measurement data $\mathbf{I}_0 \equiv \{I_{0,1}, I_{0,2}, \dots\}$, $\mathbf{I}_B \equiv \{I_{B,1}, I_{B,2}, \dots\}$, and wavelength $\boldsymbol{\lambda} \equiv \{\lambda_1, \lambda_2, \dots\}$. Using the notation $P(A|B)$ to indicate the probability of A given (or conditional on) B , Bayes' rule provides

$$P(\epsilon, \delta | \mathbf{I}_0, \mathbf{I}_B, \boldsymbol{\lambda}) \propto P(\mathbf{I}_0, \mathbf{I}_B | \epsilon, \delta, \boldsymbol{\lambda}) P_0(\epsilon, \delta). \quad (\text{A1})$$

The left side is the desired posterior probability distribution of parameters ϵ and δ given measurement data \mathbf{I}_0 , \mathbf{I}_B and $\boldsymbol{\lambda}$. The trailing term on the right side is the prior, which expresses any knowledge of ϵ and δ values before considering the measurement data. We use a prior with ϵ uniformly distributed between -0.5 and 0.5 and δ uniformly distributed between -0.5 and 0.2, reflecting a

typical reported PL contrast of 10 % to 20 % and a cursory examination of the data.

The first term on the right side of (A1) is the likelihood, the probability of obtaining data \mathbf{I}_0 and \mathbf{I}_B at wavelengths λ given parameters ϵ and δ . In the current context, the likelihood is essentially a model of spectral data as a function of the parameters, expressed as a probability distribution. To develop likelihood expressions, we construct a data model where the PL spectra are the a sum of contributions from centers in the NV^0 and NV^- charge states plus a background and noise.

$$I_{0,n} = I_n^- + I_n^0 + C + \eta_0 \quad (A2a)$$

$$I_{B,n} = (1 - \epsilon)I_n^- + (1 - \delta)I_n^0 + C + \eta_B. \quad (A2b)$$

Measurement data $I_{0,n}$ and $I_{B,n}$ are spectrum values for wavelength λ_n recorded with the magnetic field off and on, respectively. Contributions to $I_{0,n}$ from NV^- and NV^0 centers are I_n^- and I_n^0 . Parameters ϵ and δ respectively quantify quenching of the I_n^- and I_n^0 photoluminescence when the magnetic field B is applied. Wavelength-independent C is a background level, and random variables η_0 and η_B represent zero-mean, Gaussian measurement noise with standard deviations σ_0 and σ_B , respectively.

For arbitrary index n , the two equations of (A2) include two unknown values I_n^- and I_n^0 in addition to unknown parameters ϵ , δ , and C . Progress can be made if inference is limited to a few zones of the spectrum where extra information is available. Figure 7 shows the zones in relation to a sample spectrum, and the extra information applied to each zone is described below.

1. Inference procedure

a. Zone BG

The inference procedure starts by establishing the background in zone BG, which is assumed to contain measurements of C with no contribution from photoluminescence. The mean and variance of combined $I_{0,n}$ and $I_{B,n}$ data ($n \in BG$) establish a normal (Gaussian) probability distribution $P_{BG}(C)$ which is used as a prior in the next stage. To simplify notation, we define

$$P_Z(\cdot) = P(\cdot | I_{0,n}, I_{B,n}, n \in Z) \quad (A3)$$

as a parameter distribution conditional on (i.e. after inference using) all data from zone Z .

b. Zone ZPL0

Zone ZPL0 encompasses the narrow zero phonon line (ZPL) of the NV^0 , which occurs at wavelengths well below the NV^- photoluminescence spectrum. In this zone, the analysis assumes that PL data has contributions from

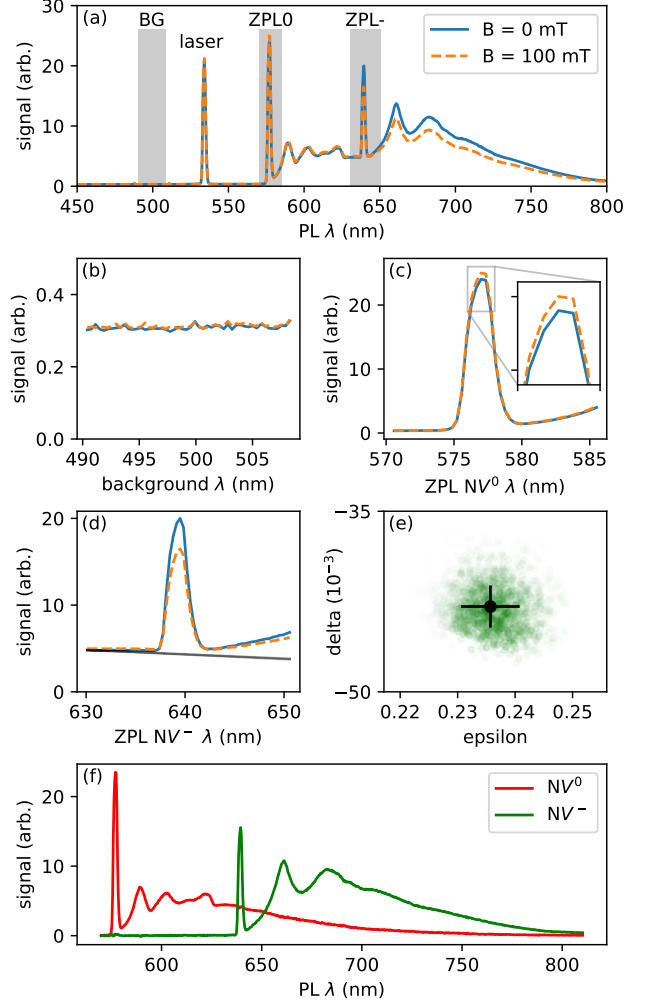


FIG. 7. Example spectra illustrating Bayesian inference methods. (a) Raw spectra collected with $40 \mu\text{W}$, 532 nm excitation at 1.6 K . The labeled grey rectangles indicate zones where data is used in Bayesian inference. The legend applies to panels (a-e). (b) Constant background in zone BG. (c) Spectra in zone ZPL0 encompassing the zero-phonon line of NV^0 . The inset highlights an increase in photoluminescence with applied field. (d) Spectra in zone ZPL- encompassing the zero-phonon line of NV^- . The black line is the inferred I^0 spectrum assuming linear wavelength dependence. The signal decreases with applied field. (e) Particle swarm representation of $P(\epsilon, \delta | \mathbf{I}_0, \mathbf{I}_B, \lambda)$. (f) Separated contributions, I^- and I^0 calculated using the mean values of ϵ and δ . The absence of a NV^- peak in the I^0 spectrum and the absence of a NV^0 peak in the I^- spectrum indicate good quality of the inference results

NV^0 and background only, so $I^-(\lambda) = 0$. Information from this zone largely determines δ .

Inference in zone ZPL0 requires a prior distribution for parameters C and δ and an expression for likelihood. For the prior, we use the product $P_0(C, \delta) = P_{BG}(C)P_0(\delta)$, which includes the background $P_{BG}(C)$ and a uniform

distribution $\delta \sim \mathcal{U}[-0.5, 0.2]$.

Manipulation of (A2a) and (A2b) to eliminate the unknown I_n^0 yields

$$(1 - \delta)I_{0,n}(\lambda) - I_{B,n}(\lambda) + \delta C = (1 - \delta)\eta_0 + \eta_B. \quad (\text{A4})$$

The terms here are arranged so that the right side has known statistical properties. (In the larger picture, the δ parameter has an unknown distribution, but for the likelihood δ is one of the given values, so it is treated as a number, not a random variable here.) The expectation (mean) $\mathcal{E}[\cdot]$ and variance $\mathcal{V}[\cdot]$ of this expression are

$$\mathcal{E}[(1 - \delta)I_{0,n}(\lambda) - I_{B,n}(\lambda) + \delta C] = 0 \quad (\text{A5})$$

$$\mathcal{V}[(1 - \delta)I_{0,n}(\lambda) - I_{B,n}(\lambda) + \delta C] = (1 - \delta)^2\sigma_0^2 + \sigma_B^2 \quad (\text{A6})$$

where σ_0 and σ_B are standard deviations expressing uncertainty in measurement data $I_{B,n}$ and $I_{B,n}$ respectively. The likelihood of measurement values $I_{B,n}$ and $I_{B,n}$ is a normal distribution

$$P(I_{0,n}, I_{B,n}|\delta, C) \propto \exp \left[\frac{-(1 - \delta)I_{0,n} - I_{B,n} + \delta C)^2}{2[(1 - \delta)^2\sigma_0^2 + \sigma_B^2]} \right]. \quad (\text{A7})$$

Application of Bayes' rule for all indices in the zone yields the posterior joint distribution $P_{\text{ZPL0}}(\delta, C)$

$$P_{\text{ZPL0}}(\delta, C) \propto \prod_{n \in \text{ZPL0}} P(I_{0,n}, I_{B,n}|\delta, C) P_0(C, \delta). \quad (\text{A8})$$

c. Zone ZPL-

Zone ZPL- encompasses the narrow ZPL peak of the NV^- spectrum, providing information to determine ϵ . The signal in this zone includes contributions from the ZPL peak of NV^- and also from the NV^0 phonon sideband. At wavelengths within zone ZPL-, I^0 is expected to be relatively featureless. We effectively assign the peak to the $I^-(\lambda)$ contribution by modeling the NV^0 contribution with as a linear function of λ , $I^0 \approx m(\lambda - \bar{\lambda}) + b$.[23, 35] Here, $\bar{\lambda}$ is chosen to be the wavelength at the center of the zone. Manipulation of (A2a) and (A2b) yields

$$(1 - \epsilon)I_{0,n} - I_{B,n} + (\epsilon - \delta)m(\lambda_n - \bar{\lambda}) + (\epsilon - \delta)b + \epsilon C = (1 - \epsilon)\eta_0 - \eta_B \quad (\text{A9})$$

the effective slope, $(\epsilon - \delta)m$ and effective $C^* = (\epsilon - \delta)b + \epsilon C$. The expectation value and variance of this expression lead to a likelihood

$$P(I_{0,n}, I_{B,n}|\epsilon, \delta, m^*, c^*) \propto \exp \left[\frac{-(1 - \epsilon)I_{0,n} - I_{B,n} + (\epsilon - \delta)m(\lambda_n - \bar{\lambda}) + (\epsilon - \delta)b + \epsilon C)^2}{2[(1 - \epsilon)^2\sigma_0^2 + \sigma_B^2]} \right] \quad (\text{A10})$$

2. Implementation

We implement the probability distributions as a particle filter / sequential Monte Carlo method. The distribution is represented by a collection of points in parameter space, $\theta_n \equiv (\epsilon_n, \delta_n, m_n, c_n)$ with weights w_n .

$$P(\theta) \approx \sum_n \delta(\theta - \theta_n)w_n. \quad (\text{A11})$$

Appendix B: PHOTODYNAMIC MODELS

The five-state model for the photodynamics of NV^- has been described by several authors.[14, 25, 36–38] In this model the ground state triplet is represented by two states: a $S_z = 0$ state and a combined $S_z = \pm 1$ state. Similarly, the excited triplet is represented by two states and the fifth state is the singlet "shelving" state. Transitions include photon absorption from ground to excited states, photon emission from excited to ground states, strongly spin-dependent relaxation from excited states

to the singlet state and slow, mildly spin-dependent relaxation from the singlet state to the ground state.

For computation, values for intrinsic relaxation rates were adopted from Tétienne et al.[37] The excitation cross sections are modeled using the form

$$\sigma_g(E_{\text{phot}}) = \sigma_0 e^{-(E_{\text{phot}} - E_{\text{max}})^2/(2w^2)}, \quad (\text{B1})$$

where σ_0 is a cross section, E_{max} is the photon energy at the maximum of the phonon band absorption and w is a width parameter. The excitation cross section of NV^- is modeled using $\sigma_0 = 0.0045 \text{ nm}^2$, $E_{\text{max}} = 2.17 \text{ eV}$ and $w = 0.21 \text{ eV}$. These values are chosen to approximate the theoretical results of Razinkoval et al.[39]. For NV^0 the values are $\sigma_0 = 0.0045 \text{ nm}^2$, $E_{\text{max}} = 2.28 \text{ eV}$ and $w = 0.21 \text{ eV}$. These values shift the phonon band by 0.21 eV (the difference in zpl energies). The unchanged σ_0 value ensures that the NV^0 cross section is 130 % of the NV^- cross section under 532 nm illumination in agreement with measurements.[25] The recombination cross section into the NV^0 excited state was arbitrarily assumed to be the same as the ionization cross section from the NV^- excited state.

[1] I. Aharonovich and E. Neu, Diamond Nanophotonics, *Advanced Optical Materials* **2**, 911 (2014).

[2] D. D. Awschalom, R. Hanson, J. Wrachtrup, and B. B. Zhou, Quantum technologies with optically interfaced solid-state spins, *Nature Photon* **12**, 516 (2018).

[3] J. F. Barry, J. M. Schloss, E. Bauch, M. J. Turner, C. A. Hart, L. M. Pham, and R. L. Walsworth, Sensitivity optimization for NV-diamond magnetometry, *Rev. Mod. Phys.* **92**, 015004 (2020).

[4] E. Bernardi, R. Nelz, S. Sonusen, and E. Neu, Nanoscale Sensing Using Point Defects in Single-Crystal Diamond: Recent Progress on Nitrogen Vacancy Center-Based Sensors, *Crystals* **7**, 124 (2017).

[5] E. Bourgeois, M. Gulka, and M. Nesladek, Photoelectric Detection and Quantum Readout of Nitrogen-Vacancy Center Spin States in Diamond, *Adv. Optical Mater.* **8**, 1902132 (2020).

[6] M. W. Doherty, N. B. Manson, P. Delaney, F. Jelezko, J. Wrachtrup, and L. C. Hollenberg, The nitrogen-vacancy colour centre in diamond, *Physics Reports* **528**, 1 (2013).

[7] F. Jelezko and J. Wrachtrup, Single defect centres in diamond: A review, *physica status solidi (a)* **203**, 3207 (2006).

[8] L. Rondin, J.-P. Tetienne, T. Hingant, J.-F. Roch, P. Maletinsky, and V. Jacques, Magnetometry with nitrogen-vacancy defects in diamond, *Reports on Progress in Physics* **77**, 056503 (2014).

[9] R. Schirhagl, K. Chang, M. Loretz, and C. L. Degen, Nitrogen-Vacancy Centers in Diamond: Nanoscale Sensors for Physics and Biology, *Annual Review of Physical Chemistry* **65**, 83 (2014).

[10] T. Schröder, S. L. Mouradian, J. Zheng, M. E. Trusheim, M. Walsh, E. H. Chen, L. Li, I. Bayn, and D. Englund, Quantum nanophotonics in diamond [Invited], *J. Opt. Soc. Am. B* **33**, B65 (2016).

[11] J. Wrachtrup and A. Finkler, Single Spin Magnetic Resonance, *Journal of Magnetic Resonance* **269**, 225 (2016), arXiv:1606.08830 [cond-mat].

[12] G. Balasubramanian, P. Neumann, D. Twitchen, M. Markham, R. Kolesov, N. Mizuochi, J. Isoya, J. Achard, J. Beck, J. Tissler, V. Jacques, P. R. Hemmer, F. Jelezko, and J. Wrachtrup, Ultralong spin coherence time in isotopically engineered diamond, *Nature Mater.* **8**, 383 (2009).

[13] T. Yamamoto, T. Umeda, K. Watanabe, S. Onoda, M. L. Markham, D. J. Twitchen, B. Naydenov, L. P. McGuinness, T. Teraji, S. Koizumi, F. Dolde, H. Fedder, J. Honert, J. Wrachtrup, T. Ohshima, F. Jelezko, and J. Isoya, Extending spin coherence times of diamond qubits by high-temperature annealing, *Phys. Rev. B* **88**, 075206 (2013).

[14] K. Beha, A. Batalov, N. B. Manson, R. Bratschitsch, and A. Leitenstorfer, Optimum Photoluminescence Excitation and Recharging Cycle of Single Nitrogen-Vacancy Centers in Ultrapure Diamond, *Phys. Rev. Lett.* **109**, 097404 (2012).

[15] G. Thiering and A. Gali, Theory of the optical spin-polarization loop of the nitrogen-vacancy center in diamond, *Phys. Rev. B* **98**, 085207 (2018).

[16] L. J. Rogers, S. Armstrong, M. J. Sellars, and N. B. Manson, Infrared emission of the NV centre in diamond: Zeeman and uniaxial stress studies, *New J. Phys.* **10**, 103024 (2008).

[17] V. M. Acosta, A. Jarmola, E. Bauch, and D. Budker, Optical properties of the nitrogen-vacancy singlet levels in diamond, *Phys. Rev. B* **82**, 201202 (2010).

[18] N. Aslam, G. Waldherr, P. Neumann, F. Jelezko, and J. Wrachtrup, Photo-induced ionization dynamics of the nitrogen vacancy defect in diamond investigated by single-shot charge state detection, *New J. Phys.* **15**, 013064 (2013).

[19] M. Goldman, A. Sipahigil, M. Doherty, N. Yao, S. Bennett, M. Markham, D. Twitchen, N. Manson, A. Kubanek, and M. Lukin, Phonon-Induced Population Dynamics and Intersystem Crossing in Nitrogen-Vacancy Centers, *Phys. Rev. Lett.* **114**, 145502 (2015).

[20] M. L. Goldman, M. W. Doherty, A. Sipahigil, N. Y. Yao, S. D. Bennett, N. B. Manson, A. Kubanek, and M. D. Lukin, State-selective intersystem crossing in nitrogen-vacancy centers, *Phys. Rev. B* **91**, 165201 (2015).

[21] M. L. Goldman, M. W. Doherty, A. Sipahigil, N. Y. Yao, S. D. Bennett, N. B. Manson, A. Kubanek, and M. D. Lukin, Erratum: State-selective intersystem crossing in nitrogen-vacancy centers [Phys. Rev. B **91**, 165201 (2015)], *Phys. Rev. B* **96**, 039905 (2017).

[22] D. M. Toyli, D. J. Christle, A. Alkauskas, B. B. Buckley, C. G. Van de Walle, and D. D. Awschalom, Measurement and Control of Single Nitrogen-Vacancy Center Spins above 600 K, *Phys. Rev. X* **2**, 031001 (2012).

[23] D. Aude Craik, P. Kehayias, A. Greenspon, X. Zhang, M. Turner, J. Schloss, E. Bauch, C. Hart, E. Hu, and R. Walsworth, Microwave-Assisted Spectroscopy Technique for Studying Charge State in Nitrogen-Vacancy Ensembles in Diamond, *Phys. Rev. Applied* **14**, 014009 (2020).

[24] D. A. Hopper, R. R. Grote, A. L. Exarhos, and L. C. Bassett, Near-infrared-assisted charge control and spin readout of the nitrogen-vacancy center in diamond, *Phys. Rev. B* **94**, 241201 (2016).

[25] L. Hacquebard and L. Childress, Charge-state dynamics during excitation and depletion of the nitrogen-vacancy center in diamond, *Phys. Rev. A* **97**, 063408 (2018).

[26] S. A. Wolf, I. Meirzada, G. Haim, and N. Bargill, Nitrogen-vacancy singlet manifold ionization energy (2022), arXiv:2210.04171 [quant-ph].

[27] G. R. Eaton, S. S. Eaton, D. P. Barr, and R. T. Weber, *Quantitative EPR* (Springer Vienna, Vienna, 2010).

[28] A. M. Edmonds, C. A. Hart, M. J. Turner, P.-O. Colard, J. M. Schloss, K. S. Olsson, R. Trubko, M. L. Markham, A. Rathmill, B. Horne-Smith, W. Lew, A. Manickam, S. Bruce, P. G. Kaup, J. C. Russo, M. J. DiMario, J. T. South, J. T. Hansen, D. J. Twitchen, and R. L. Walsworth, Characterisation of CVD diamond with high concentrations of nitrogen for magnetic-field sensing applications, *Mater. Quantum. Technol.* **1**, 025001 (2021).

[29] S. Felton, A. M. Edmonds, M. E. Newton, P. M. Martineau, D. Fisher, and D. J. Twitchen, Electron paramagnetic resonance studies of the neutral nitrogen vacancy in diamond, *Phys. Rev. B* **77**, 081201 (2008).

[30] M. S. Barson, E. Krausz, N. B. Manson, and M. W. Doherty, The fine structure of the neutral nitrogen-vacancy

center in diamond, *Nanophotonics* **8**, 1985 (2019).

[31] S. Stoll and A. Schweiger, EasySpin, a comprehensive software package for spectral simulation and analysis in EPR, *Journal of Magnetic Resonance* **178**, 42 (2006).

[32] J. H. N. Loubser and J. A. v. Wyk, Electron spin resonance in the study of diamond, *Rep. Prog. Phys.* **41**, 1201 (1978).

[33] W. V. Smith, P. P. Sorokin, I. L. Gelles, and G. J. Lasher, Electron-Spin Resonance of Nitrogen Donors in Diamond, *Phys. Rev.* **115**, 1546 (1959).

[34] C. Glover, M. E. Newton, P. Martineau, D. J. Twitchen, and J. M. Baker, Hydrogen Incorporation in Diamond: The Nitrogen-Vacancy-Hydrogen Complex, *Phys. Rev. Lett.* **90**, 185507 (2003).

[35] T. Chakraborty, R. Bhattacharya, V. Anjusha, M. Nesseladek, D. Suter, and T. Mahesh, Magnetic-Field-Assisted Spectral Decomposition and Imaging of Charge States of N - V Centers in Diamond, *Phys. Rev. Applied* **17**, 024046 (2022).

[36] L. Robledo, H. Bernien, T. v. d. Sar, and R. Hanson, Spin dynamics in the optical cycle of single nitrogen-vacancy centres in diamond, *New Journal of Physics* **13**, 025013 (2011).

[37] J.-P. Tetienne, L. Rondin, P. Spinicelli, M. Chipaux, T. Debuisschert, J.-F. Roch, and V. Jacques, Magnetic-field-dependent photodynamics of single NV defects in diamond: an application to qualitative all-optical magnetic imaging, *New J. Phys.* **14**, 103033 (2012).

[38] G. Liaugaudas, G. Davies, K. Suhling, R. U. A. Khan, and D. J. F. Evans, Luminescence lifetimes of neutral nitrogen-vacancy centres in synthetic diamond containing nitrogen, *J. Phys.: Condens. Matter* **24**, 435503 (2012).

[39] L. Razinkovas, M. Maciaszek, F. Reinhard, M. W. Doherty, and A. Alkauskas, Photoionization of negatively charged NV centers in diamond: Theory and *ab initio* calculations, *Phys. Rev. B* **104**, 235301 (2021).

[40] E. Bourgeois, E. Londero, K. Buczak, J. Hruby, M. Gulka, Y. Balasubramaniam, G. Wachter, J. Stursa, K. Dobes, F. Aumayr, M. Trupke, A. Gali, and M. Nesseladek, Enhanced photoelectric detection of NV magnetic resonances in diamond under dual-beam excitation, *Phys. Rev. B* **95**, 041402 (2017).

[41] L. J. Rogers, R. L. McMurtrie, M. J. Sellars, and N. B. Manson, Time-averaging within the excited state of the nitrogen-vacancy centre in diamond, *New J. Phys.* **11**, 063007 (2009).

[42] P. Tamarat, N. B. Manson, J. P. Harrison, R. L. McMurtrie, A. Nizovtsev, C. Santori, R. G. Beausoleil, P. Neumann, T. Gaebel, F. Jelezko, P. Hemmer, and J. Wrachtrup, Spin-flip and spin-conserving optical transitions of the nitrogen-vacancy centre in diamond, *New J. Phys.* **10**, 045004 (2008).

[43] A. Batalov, V. Jacques, F. Kaiser, P. Siyushev, P. Neumann, L. J. Rogers, R. L. McMurtrie, N. B. Manson, F. Jelezko, and J. Wrachtrup, Low Temperature Studies of the Excited-State Structure of Negatively Charged Nitrogen-Vacancy Color Centers in Diamond, *Phys. Rev. Lett.* **102**, 195506 (2009).

[44] K.-M. C. Fu, C. Santori, P. E. Barclay, L. J. Rogers, N. B. Manson, and R. G. Beausoleil, Observation of the Dynamic Jahn-Teller Effect in the Excited States of Nitrogen-Vacancy Centers in Diamond, *Phys. Rev. Lett.* **103**, 256404 (2009).

[45] J. Happacher, D. A. Broadway, J. Bocquel, P. Reiser, A. Jimenéz, M. A. Tschudin, L. Thiel, D. Rohner, M. I. G. Puigibert, B. Shields, J. R. Maze, V. Jacques, and P. Maletinsky, Low-Temperature Photophysics of Single Nitrogen-Vacancy Centers in Diamond, *Phys. Rev. Lett.* **128**, 177401 (2022).

[46] S. Ernst, P. J. Scheidegger, S. Diesch, L. Lorenzelli, and C. L. Degen, Temperature dependence of photoluminescence intensity and spin contrast in nitrogen-vacancy centers (2023), arXiv:2301.05091 [cond-mat, physics:quant-ph].